

Extended temperature regions of multiferroicity in nanoscale CuO

Jacob M. Schliesser, Rebecca E. Olsen, and Brian F. Woodfield*

Brigham Young University, Provo, UT 84602, USA

*Corresponding author: Brian F. Woodfield

Tel.: +1 801 422 2093

Fax: +1 801 422 0153

Address: C100 BNSN, Dept. of Chemistry and Biochemistry, Brigham Young University, Provo, UT 84602

E-mail address: Brian_Woodfield@byu.edu

ABSTRACT

We have measured the magnetic susceptibility and heat capacity of CuO nanoparticles (16 nm) from 2 K to 400 K using a Quantum Design Physical Properties Measurement System (PPMS). The magnetization curves, acquired at various field strengths from 0 Oe to 50 kOe, are similar to literature data of bulk and nanoscale CuO showing a minimum at about 150 K, an upturn as temperature approaches 0 K, and a broad maximum at high temperatures extending beyond 400 K. The heat capacity data between 200 K and 400 K show several broad peaks. The number of these peaks and the temperatures at which they occur differ significantly from the magnetic transitions known to exist in bulk CuO. To further investigate these transitions in nanoscale CuO, we performed temperature dependent x-ray diffraction (XRD) at temperatures from 90 K to 700 K from which lattice parameters as a function of temperature were derived using a Rietveld refinement. Although no phase transitions were observed in these data, changes in the slopes of the lattice parameters are apparent at the transition temperatures observed in the heat capacity and susceptibility measurements. The various transitions in the heat capacity data are attributed to competing ferromagnetic and antiferromagnetic interactions caused by structural properties that are unique to nanophase CuO, and the temperature range of multiferroicity in nanoscale CuO is shown to extend to temperatures higher than those observed for bulk CuO. The heat capacity and temperature dependent XRD measurements are the first of their kind to be reported for CuO nanoparticles.

Keywords: cupric oxide, tenorite, nanoparticle, magnetization, specific heat, X-ray diffraction

1. Introduction

Cupric oxide, CuO (tenorite), has been extensively studied due to its significance in basic science as well as technological applications. CuO has unique structural and magnetic properties [1; 2; 3], and it is closely related to the high-temperature superconducting cuprates such as $\text{YBa}_2\text{Cu}_3\text{O}_{7-x}$ [4]. In terms of applications, it has use in catalysis [5], photovoltaics [6; 7; 8], batteries [9], and potential uses in spintronic devices [10; 11; 12],

CuO is unique for a $3d$ transition-metal monoxide having a $C2/c$ monoclinic structure instead of the rock salt structure common to the other $3d$ transition-metal oxides [13; 14]. The Cu atom is surrounded by four O atoms in a square planar configuration which can be viewed as edge-shared ribbon chains of CuO_2 or as two zigzag Cu–O chains running along the $[101]$ and $[10\bar{1}]$ directions (see Figure 1) [10; 15]. These chains are what make CuO important in cuprate superconductor research since the cuprate superconductors also have CuO_2 chains [4; 10; 16; 17; 18].

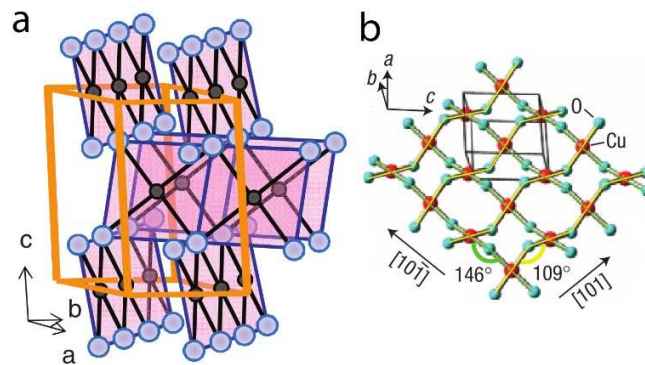


Figure 1. Structure of CuO showing a) edge-shared ribbon chains of CuO_2 (from Wu *et al.* [15] with permission) and b) zigzag chains along the $[101]$ (yellow lines) and $[10\bar{1}]$ (green lines) directions (from Kimura *et al.* [10] with permission).

The magnetic behavior of CuO is also unique relative to the other 3d transition-metal monoxides which all behave as 3D antiferromagnets; whereas, CuO exhibits various forms of magnetism within different temperature ranges [19; 20]. Heat capacity measurements on bulk CuO performed by many groups [2; 3; 4; 18; 21; 22; 23; 24; 25; 26; 27; 28; 29] show two distinct magnetic transitions at about 213 and 230 K. The peak at 213 K has been attributed to a transition from a 3D commensurate antiferromagnetic state below 213 K (AF1) to a 3D incommensurate state above 213 K (AF2). The peak at 230 K has been attributed to a transition from the AF2 state to a 1D antiferromagnetic state above 230 K. Heat capacity measurements have not previously been performed on nanoscale CuO.

Magnetic susceptibility data of bulk [1; 3; 4; 10; 11; 12; 24; 30; 31] and nanoscale [32; 33; 34] CuO are similar to each other and show neither a cusp at the temperatures of the transitions observed in heat capacity data nor typical Curie-Weiss behavior. Instead, a broad maximum at about 540 K and a minimum at about 150 K are observed. The only evidence of any transitions in the range of (213-230) K from susceptibility data is a subtle change in slope [3; 4; 10; 34].

Neutron experiments have provided more details about the magnetic character of bulk CuO in the various temperature regions and show that the incommensurate AF2 state occurs because of competing ferromagnetic and antiferromagnetic interactions [11; 16; 17; 30; 35; 36; 37]. Figure 2 shows the orientation of the spins in the commensurate AF1 and incommensurate AF2 states [10]. The direction of the easy axis is along b [19; 37], and the strongest antiferromagnetic ordering occurs along the $[10\bar{1}]$ chains because of the large Cu–O–Cu angle (146°) [16; 17]. Super exchange interactions along the other directions are very weak (either ferromagnetically or antiferromagnetically) due to the smaller bond angles (less than 109°) [17;

38]. In the AF1 state the spins align parallel to b with a wave propagation vector of $\mathbf{q}_{\text{cm}} = (0.5, 0, -0.5)$, and in the AF2 state, the wave propagation vector is $\mathbf{q}_{\text{icm}} = (0.506, 0, -0.483)$ having a helical spin structure such that the Cu^{2+} moments nearly circle in a plane [12]. To the best of our knowledge, no neutron experiments have investigated the magnetic character of nanoscale CuO.

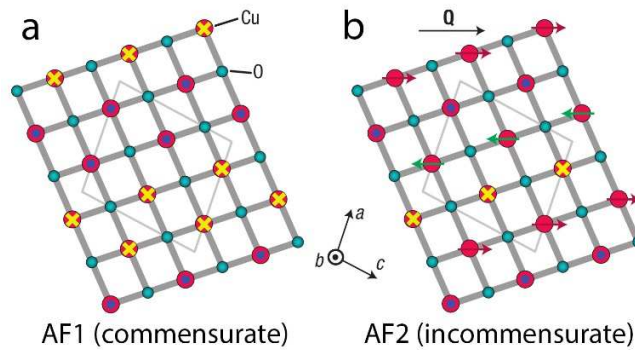


Figure 2. Magnetic structure of the a) AF1 (commensurate) and b) AF2 (incommensurate) phases (from Kimura *et al.* [10] with permission).

As seen from magnetization measurements, the susceptibility continues to increase above the Néel temperature T_{N2} of 230 K, which would be atypical behavior for paramagnetism [39]. Super paramagnetism and a spin-glass state from surface spins have been ruled out as the cause for this observed behavior [33]. Neutron experiments have failed to detect paramagnetism in bulk CuO even at temperatures as high 550 K [36] but have shown that antiferromagnetism persists above T_{N2} in a 1D form [2; 3; 4; 16; 17; 40]. This is thought to occur through the very large super exchange interactions along the $[10\bar{1}]$ direction having an exchange constant in the range of 35-73 meV, which is much larger than exchange constants of other ionic antiferromagnets (typically less than 10 meV) [17; 32; 38; 40].

More recently, multiferroic behavior, which is the coexistence of magnetism and ferroelectricity, has been discovered within the AF2 state of bulk CuO [10]. Due to the competing interactions involved in spiral-phase-induced ferroelectricity, multiferroicity is typically only observed below about 40 K making it inaccessible to practical technological applications [10; 11]. The relatively high temperature of multiferroicity in CuO (230 K) has spurred many recent investigations [10; 11; 12; 19; 20]. Because CuO is a core component of many high-temperature superconductors, understanding the origins of its multiferroic behavior could lead to a greater understanding of superconductivity and even drive the discovery or creation of superconductors with higher critical temperatures than current materials. The high-temperature multiferroic behavior of CuO could also be used in sensors, memory devices, and magnetoelectric devices [41].

All of the physical properties discussed above have been extensively investigated for bulk CuO, but there have been minimal investigations of nanoscale CuO [32; 33; 34; 42; 43; 44]. This paper will present heat capacity, susceptibility, and temperature dependent XRD data on nanoscale CuO that have not been reported previously in the literature thus providing an extensive investigation on the magnetic and structural properties of CuO nanoparticles. We will show that structural features common to nanoparticles are responsible for extending the magnetic and ferroelectric temperature ranges by creating stronger ferromagnetic and antiferromagnetic competition through increased exchange interactions along the various directions.

2. Experimental

2.1. Synthesis and characterization

CuO nanoparticles were prepared using a solvent deficient method developed by Woodfield *et al.* [45] in which 53 g of $\text{Cu}(\text{NO}_3)_2 \cdot 2.5\text{H}_2\text{O}$, 38 g of NH_4HCO_3 , and 10 mL of H_2O

were ground together in a mortar and pestle for approximately 1 min. The formed precursor was rinsed with about 0.5 L of distilled H₂O and then calcined in air at 250 °C for 1 h. Table 1 shows the sample properties and purity.

Chemical	Source	Fraction Purity	Purification Method	Analysis Method
Cu(NO ₃) ₂ ·2.5H ₂ O	Sigma	>0.98	None; used as received	
NH ₄ HCO ₃	Sigma	>0.99	None; used as received	
CuO·0.05H ₂ O	Synthesized	>0.98	Calcination	PXRD ^a , TGA ^b , TEM ^c

^aPowder X-Ray Diffraction

^bThermal Gravimetric Analysis

^cTransmission Electron Microscopy

Table 1. CuO sample description, properties, and purity

Transmission electron microscopy (TEM) imaging was carried out using several techniques (see Figure 3). The bright field image (Figure 3a) shows ellipsoidal crystallites that are highly agglomerated into much larger particles. The high-resolution image (Figure 3b) shows that the sample is highly crystalline as lattice fringes are abundantly observed. This figure also shows the presence of a secondary CuO particle size of about 5 nm, though these particles represent only a small fraction of the sample. Diffraction techniques were also used, and the absence of any pronounced amorphous background intensity in the acquired diffraction pattern (Figure 3c) shows the high degree of crystallinity. The hollow cone dark field image (Figure 3d) shows that the particles are about 20 nm in diameter, though the slightly ellipsoidal shape introduces uncertainty to this value.

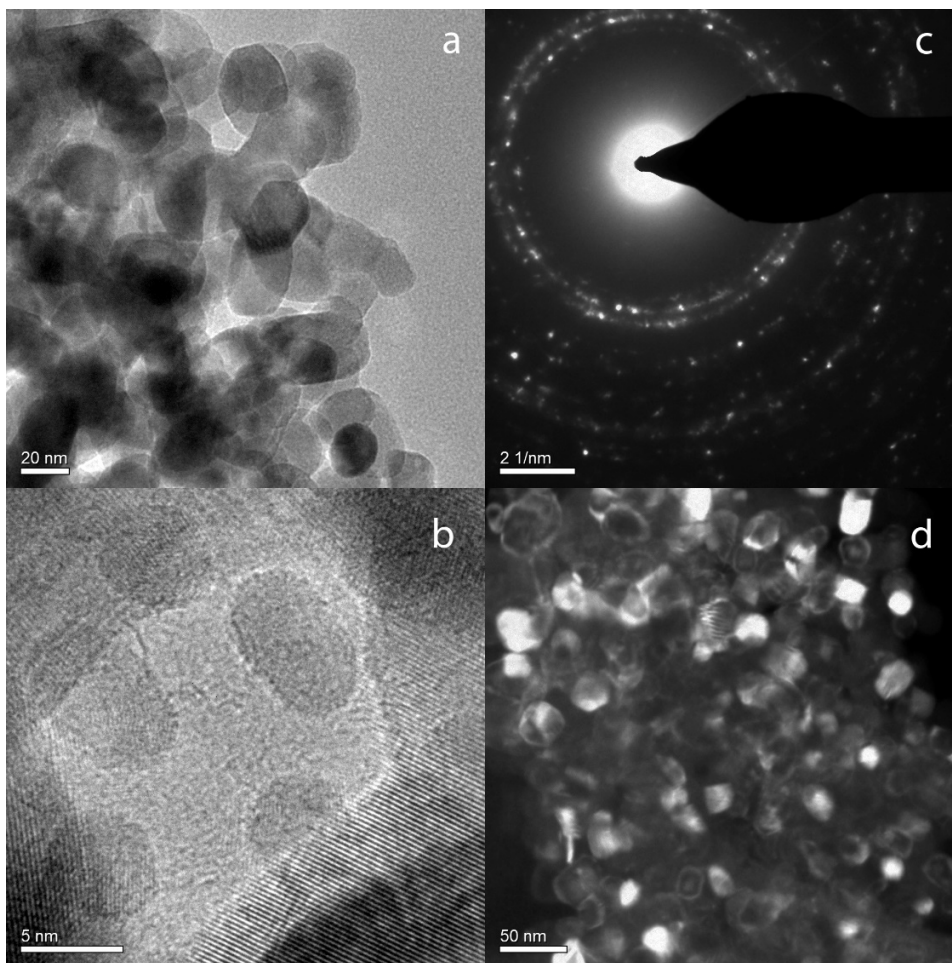


Figure 3. TEM images and diffraction patterns of CuO nanoparticles. a) bright field. b) high-resolution. c) diffraction pattern. d) hollow cone dark field.

The amount of surface-adsorbed water was determined by thermogravimetric analysis (TGA) using a Netzsch STA-409 PC. Prior to the TGA measurements, the sample was dried in a vacuum oven ($p = 16.2$ kPa) at 100 °C for about 3 h to remove all loosely bound physisorbed water that would be removed during the heat capacity measurements under high vacuum. The TGA measurements were performed under a helium atmosphere with temperatures of 20 - 900 °C using a heating rate of 3 °C \cdot min $^{-1}$. A buoyancy correction was made by measuring the empty crucible under the same conditions and subtracting this from the measured data. The weight loss

at the inflection point of about 500 °C (see Figure 4) was attributed to the desorption of chemisorbed water, and the amount of water was determined to be 0.050 ± 0.004 moles of H₂O per mole of CuO. The TGA-DSC data presented in Figure 4 show that nanoscale CuO is reduced at about 800 °C.

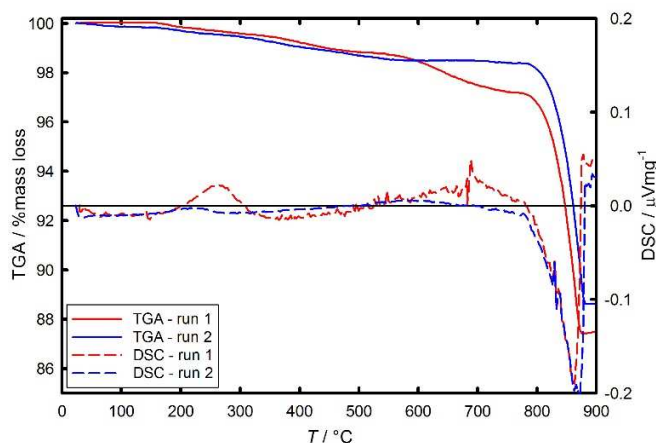


Figure 4. TGA-DSC data of CuO nanoparticles showing mass loss due to water desorption up to about 500 °C and reduction above about 800 °C. The left axis gives the percent mass and is represented with solid lines. The right axis gives the DSC data and is represented with dashed lines. The solid black line corresponds to $0 \mu\text{V}\cdot\text{mg}^{-1}$ for the DSC axis. red – run 1; blue – run 2.

2.2. Magnetometry

Magnetization curves from 5-400 K were acquired on a Quantum Design Physical Property Measurement System (PPMS) using the vibrating sample magnetometer (VSM) option. The sample was cooled in zero field to about 5 K, and the magnetic moment as a function of temperature was measured in various external field strengths: (0, 50, 100, 1,000, 10,000, and 50,000) Oe.

2.3. X-ray diffraction

Phase purity was confirmed with X-ray diffraction (XRD) using a PANalytical X'Pert Pro X-ray diffractometer with a Cu K α radiation source ($\lambda = 0.15418$ nm) operating at 45 kV and 40 mA. Data were recorded over a 2θ range of $(20-125)^\circ$ with a scanning rate of $0.01^\circ \cdot \text{s}^{-1}$. Only monoclinic CuO was observed; however, a Reitveld refinement of this data reveals that significant lattice vacancies are present [46]. Particle size was determined to be about 16 nm using the Scherrer formula, which is slightly smaller than the sizes obtained from the TEM images, but since the XRD data analyze significantly more particles than the TEM imaging, we will consider the particles to be 16 nm in diameter.

XRD data were also acquired at various temperatures from 90-700 K in order to determine the lattice parameters as a function of temperature. Data above room temperature were collected on the PANalytical X'Pert Pro powder X-ray diffractometer using an Anton Paar HTK 1200N heating stage. Data were collected every 25 K from (300-700) K using the same parameters as described above.

To measure the XRD data below room temperature, we used a single crystal (SC) Bruker diffractometer equipped with a cold finger as described previously [46]. In brief, the powder sample was uniformly compacted into a polyamide capillary having an inner diameter of 0.012 mm, and the ends of the capillary were sealed with clay due to its amorphicity. The sample was mounted on the SC-XRD, and data were collected at temperatures from (90-295) K over 2θ scanning angles of $(20-130)^\circ$. Data were collected about every 25 K below 195 K and about every 15 K from (195-295) K.

2.4. Heat capacity calorimetry

Heat capacities were measured from (2-400) K using the Quantum Design PPMS. To prepare the sample for measurement, about 9 mg of the dried sample mixed with high purity copper (mass fraction 0.9995) were pressed into a small disk [47]. Correction measurements were performed before each sample measurement to account for the Apiezon N grease used for mounting the sample at low temperatures (below 300 K) and the Apiezon H grease used for mounting the sample at high temperatures (above about 250 K). After each of these correction measurements the sample was attached to the PPMS puck, and the heat capacity was measured. The heat capacity of the copper contribution was subtracted using data from Stevens and Boerio-Goates [48]. These data have an estimated expanded, combined uncertainty of $\pm 0.06 \cdot C_p^\circ$ for $2 < T/K < 10$ and $\pm 0.01 \cdot C_p^\circ$ for $10 < T/K < 300$ at approximately 95% confidence limits [47]. The high temperature ($T/K > 300$) uncertainty of this method has not been previously characterized. Based on the region of overlap between the low temperature and high temperature data sets, we estimate that the expanded, combined uncertainty of the $300 < T/K < 400$ region is approximately $\pm 0.02 \cdot C_p^\circ$ at ~95% confidence limits.

3. Results and discussion

3.1. Magnetization

Magnetic susceptibility measurements were performed on the nanoscale CuO sample at various external field strengths; these are tabulated in Table 2 and shown in Figure 5. The data show a minimum at about (100-150) K, a sharp up-turn as temperature decreases towards 0 K, and an increase towards an apparent maximum above 400 K. Several small features are observed at various temperatures, but we believe these are due to noise in the data.

T / K	$X(0 \text{ Oe}) / 10^{-6} \cdot \text{emu} \cdot \text{g}^{-1}$	$X(50 \text{ Oe}) / 10^{-6} \cdot \text{emu} \cdot \text{g}^{-1}$	$X(100 \text{ Oe}) / 10^{-6} \cdot \text{emu} \cdot \text{g}^{-1}$	$X(1 \text{ kOe}) / 10^{-6} \cdot \text{emu} \cdot \text{g}^{-1}$	$X(10 \text{ kOe}) / 10^{-6} \cdot \text{emu} \cdot \text{g}^{-1}$	$X(50 \text{ kOe}) / 10^{-6} \cdot \text{emu} \cdot \text{g}^{-1}$
---------	--	---	--	---	--	--

	1	1		1	1	1
5.90	0.954	1.34	4.06	1870	163000	577000
8.78	0.639	0.774	2.30	1160	94900	314000
12.8	0.387	0.496	1.52	739	56600	178000
16.8	0.275	0.334	1.08	500	40500	114000
20.7	0.217	0.255	0.886	366	32000	85500
24.7	0.185	0.226	0.720	267	25800	73400
28.7	0.125	0.180	0.544	216	21400	56100
32.8	0.105	0.154	0.492	178	17900	41400
36.8	0.109	0.164	0.399	155	15000	17400
40.8	0.0701	0.127	0.357	134	12800	14900
44.8	0.0474	0.109	0.279	127	11100	9110
48.8	0.0405	0.0807	0.268	120	10100	9800
52.8	0.0232	0.0635	0.225	112	9340	7230
56.8	0.0170	0.0545	0.230	108	8620	10600
60.7	0.00838	0.0471	0.189	98.1	8290	11900
64.9	0.00464	0.0325	0.178	100	7830	12500
69.1	0.00614	0.0246	0.160	95.7	7470	10500
73.00	0.00335	0.0341	0.134	86.4	7040	9010
77.2	0.00218	0.0153	0.120	87.9	6790	10800
81.1	0.00223	0.0143	0.0820	85.3	6490	11900
85.1	0.00195	0.0104	0.0682	84.2	6310	11900
89.1	0.00124	0.0069	0.0543	81.5	6100	16200
93.1	0.00126	0.00760	0.0552	73.8	5560	17300
97.1	0.000578	0.00589	0.0460	73.2	5380	17000
101	1.72E-07	0.00991	0.0542	74.2	5490	12900
105	0.0000528	0.00596	0.0492	71.3	5380	10400
109	0.000440	0.00572	0.0498	68.9	5110	12300
113	0.000296	0.00595	0.0503	66.9	4920	11700
118	0.000571	0.00146	0.0312	65.8	4860	10600
122	0.00175	0.000674	0.0399	64.5	4740	10700
126	0.000692	0.000159	0.0473	63.4	4660	11100
130	0.00116	0.0000891	0.0512	62.8	4620	11600
134	0.00348	0.0000693	0.0573	62.1	4620	12500
138	0.00664	0.0000285	0.0483	61.7	4600	13500
142	0.00421	0.000155	0.0489	60.9	4580	14200
146	0.00695	0.000243	0.0612	60.7	4590	15100
150	0.00688	0.000139	0.0573	60.7	4590	15300
154	0.00640	0.000182	0.0528	61.2	4560	15700
158	0.00651	0.000120	0.0511	61.1	4560	16400
162	0.00623	0.000745	0.0504	60.4	4560	17100
166	0.0115	0.000234	0.0538	59.5	4580	18200
170	0.0125	0.000400	0.0527	59.8	4620	19000
174	0.0258	0.000109	0.0536	60.5	4680	19700

178	0.0385	0.0000812	0.0670	61.3	4750	20600
182	0.0405	0.000551	0.0627	61.7	4770	21700
186	0.0192	0.00122	0.0681	62.0	4780	22400
191	0.0103	0.000433	0.0762	63.3	4760	23400
195	0.00518	0.000585	0.0786	63.1	4920	24400
199	0.00313	0.00489	0.092	64.8	5020	25800
204	0.00183	0.0130	0.130	65.8	5110	26800
209	0.00460	0.0185	0.150	67.0	5200	28700
213	0.00747	0.0209	0.152	68.0	5310	30800
217	0.0105	0.0197	0.170	68.9	5410	32400
221	0.0116	0.0231	0.170	70.5	5510	33900
225	0.0187	0.0238	0.175	70.8	5590	35500
229	0.0342	0.0240	0.175	71.3	5680	36800
233	0.0340	0.0284	0.194	71.8	5740	38200
237	0.0337	0.0297	0.197	72.5	5770	39600
241	0.0336	0.0338	0.207	72.6	5810	40700
245	0.0410	0.0343	0.206	73.0	5810	42200
249	0.0441	0.0399	0.210	73.1	5830	43800
253	0.0217	0.0483	0.232	73.3	5840	44600
257	0.00290	0.0516	0.267	73.0	5840	45400
261	0.00155	0.0542	0.258	72.4	5830	46000
265	0.00279	0.0605	0.249	72.2	5820	47200
269	0.00154	0.0555	0.256	72.0	5820	48300
273	0.00174	0.0580	0.261	71.7	5800	48900
277	0.00261	0.0544	0.253	71.5	5810	49700
281	0.000877	0.0559	0.260	71.3	5790	50900
285	0.00192	0.0543	0.267	71.5	5780	51800
289	0.00188	0.0591	0.286	71.4	5730	53000
293	0.00297	0.0624	0.274	71.1	5770	54000
297	0.00166	0.0632	0.274	71.0	5790	55300
301	0.00337	0.0669	0.281	70.2	5790	55700
305	0.00207	0.0622	0.275	70.0	5750	56700
309	0.00150	0.0699	0.284	70.0	5750	57600
313	0.00218	0.0573	0.289	69.3	5740	58300
317	0.00144	0.0635	0.293	69.2	5710	59400
321	0.00176	0.0651	0.299	68.9	5700	60600
325	0.00195	0.0609	0.288	68.5	5700	61600
329	0.00267	0.0661	0.304	68.2	5690	62600
333	0.00316	0.0599	0.292	68.0	5680	63900
337	0.00199	0.0609	0.311	67.7	5660	65200
341	0.00127	0.0635	0.302	67.8	5650	66400
345	0.00175	0.0681	0.304	67.4	5640	67500
349	0.000801	0.0590	0.304	66.9	5630	68600
353	0.000976	0.0602	0.317	66.8	5620	69500
357	0.000861	0.0650	0.308	66.4	5600	70400

361	0.00167	0.0659	0.307	66.1	5590	71700
365	0.00173	0.0663	0.302	66.1	5600	72900
369	0.00195	0.0688	0.296	66.0	5610	74000
373	0.00102	0.0655	0.297	65.9	5610	75200
377	0.000391	0.0711	0.299	65.6	5600	76300
381	0.000790	0.0717	0.316	65.2	5600	77300
385	0.000691	0.0769	0.292	65.2	5590	78300
389	0.000755	0.0829	0.306	65.0	5570	79200
393	0.000443	0.0850	0.303	64.7	5550	80100
397	0.000268	0.0758	0.307	64.4	5520	81100
401	0.000785	0.0664	0.321	64.4	5520	82100

The estimated standard uncertainty in the temperature T is $u(T) = 0.001 \cdot T/K$. The expanded, combined uncertainties at approximately 95 percent confidence limits in the values of X are $U(X) = 0.05 \cdot X$.

Table 2. Measured magnetic susceptibility data at constant pressure ($p = 1.2$ mPa) for CuO.

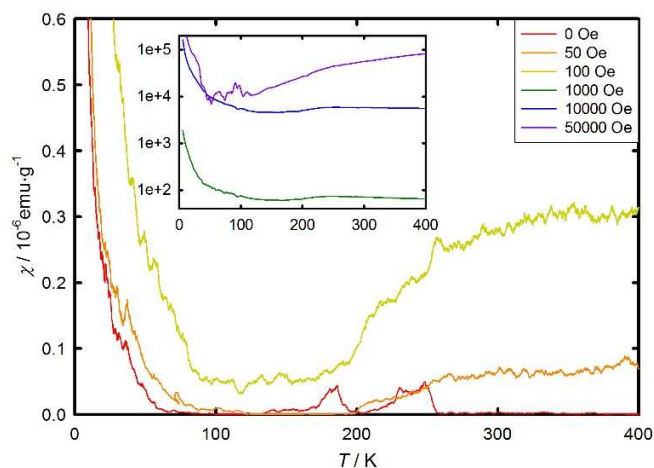


Figure 5. ZFC gram susceptibility of nanoscale CuO as determined from VSM measurements.

Data were taken under various external magnetic fields: red – 0 Oe; orange – 50 Oe; yellow – 100 Oe; green – 1,000 Oe; blue – 10,000 Oe; purple – 50,000 Oe. Note the log scale on the inset.

Although these data do not follow the traditional Curie-Weiss behavior, these trends and features have been observed several times before for both bulk and nanoscale CuO, and Figure 6 shows our measured susceptibility data (at 100 Oe scaled by a factor of 5) relative to literature

data for bulk [1; 3; 4; 11; 30] and nanoscale [32] CuO. We note that the susceptibility data of our nanoscale CuO collected in fields of 100 Oe or less are significantly lower in magnitude than the literature data of bulk and nanoscale CuO; conversely, our data collected in fields of 1,000 Oe or more are significantly higher in magnitude. Perhaps this discrepancy is due to the use of VSM as opposed to other magnetization techniques. Additionally, the up-turn at low temperatures in our data is much more prominent and larger in magnitude compared to the literature data as well. Other than the difference in magnitude of the susceptibility and the large up-turn at low temperatures, our data have the same general trends as the literature.

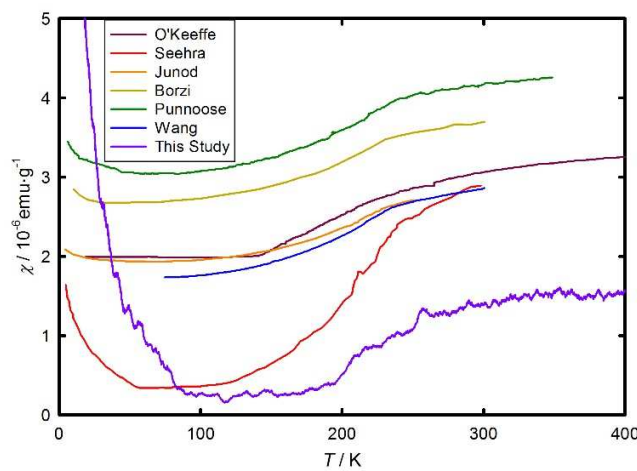


Figure 6. Comparison of the susceptibility data of nanoscale CuO presented herein (100 Oe data scaled by a factor of 5) to data obtained from various literature studies of bulk and nanoscale CuO [1; 3; 4; 11; 30; 32].

The low-temperature upturn in our susceptibility data is similar to that of other bulk and nanoscale CuO samples and has been attributed to small particle size [1] and non-ideal stoichiometry such as oxygen vacancies [31], though the underlying cause of the up-turn from

both size and stoichiometry effects is the same: paramagnetic sites on the particle surface or around vacancies. The larger up-turn in our sample is likely caused by the presence of both of these sources of paramagnetic centers (small particle size and non-ideal stoichiometry) in our nanoscale CuO sample. A large concentration of paramagnetic sites would also explain why the magnitude of the antiferromagnetic susceptibility tends to be lower than the literature.

An alternate explanation for the large up-turn in our nanoscale CuO could be the presence of stronger ferromagnetic interactions, which yield a similar feature in the susceptibility to that observed in our susceptibility data in Figure 5. Small particle sizes and lattice vacancies have been shown to create a small ferromagnetic contribution in both bulk and nanoscale CuO [32; 33; 34]. The super exchange interactions along [101] and [010] are known to be weakly ferromagnetic [2]; therefore, the presence of ferromagnetism at low temperatures in nanoscale CuO would likely be caused by changes in Cu–O–Cu bond lengths and angles that enhance the exchange interactions in these directions.

3.2. XRD lattice parameters

The XRD data of nanoscale CuO at temperatures from (90-700) K are shown in Figure 7. The high-temperature data (Figure 7a) show a weaker signal-to-noise ratio than the low-temperature data (Figure 7b), but the instrumental broadening of the low-temperature data is more significant as seen by the broader peaks, which is caused by using transmitted X-rays as opposed to reflected X-rays. These data show that the sample is highly crystalline and phase pure over the entire temperature range. A subtle shift towards sharper and more defined peaks at higher temperatures suggests that the particles are becoming more crystalline or larger, which would reduce peak broadening from microstrain and size effects.

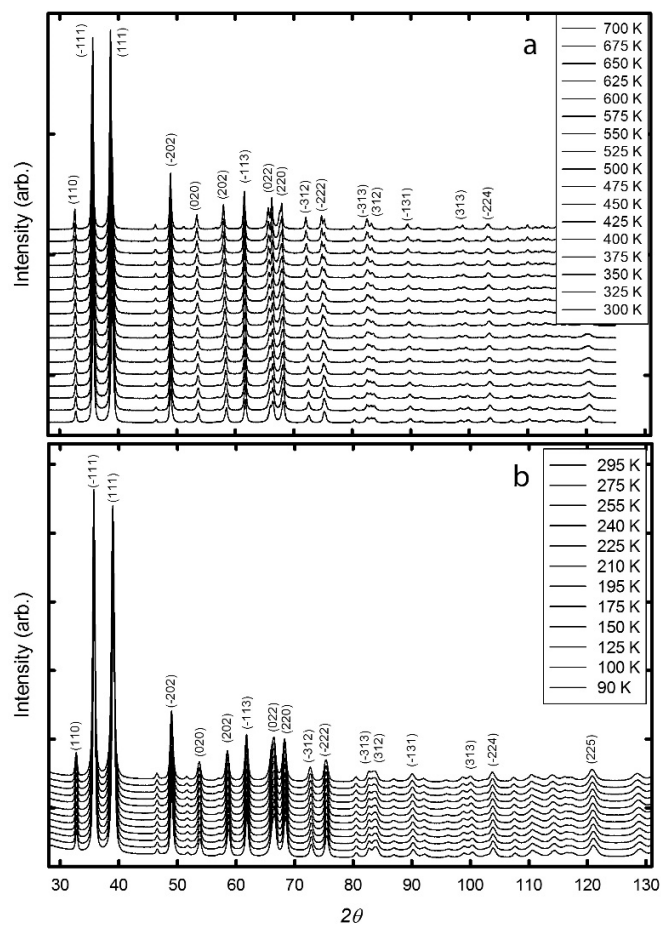


Figure 7. XRD data of nanoscale CuO at various temperatures from 90-700 K. a) high-temperature data (300-700 K) collected on the powder diffractometer. b) low-temperature data (90-295 K) collected on the single-crystal diffractometer. Data (offset for clarity) increase in temperature from bottom to top as shown in the legends.

We have performed a Rietveld refinement on the data shown in Figure 7 to obtain lattice parameters at the various temperatures, which are given in Table 3 and shown in Figure 8, and we note that our data are in good agreement with the literature data collected at room temperature for bulk and nanoscale CuO [4; 11; 13; 14]. To the best of our knowledge, though, this is the first investigation to show the progression of lattice parameters as a function of

temperature for either bulk or nanoscale CuO. Although there are no phase transitions in which lattice parameters change abruptly, changes in the slope of the data at various temperatures are apparent. We also note that these changes occur at different temperatures for each of the different lattice parameters.

Temp / °C	a / Å	b / Å	c / Å	β / °
90	4.6769	3.4198	5.1242	99.600
100	4.6772	3.4200	5.1242	99.595
125	4.6773	3.4204	5.1248	99.590
150	4.6775	3.4208	5.1252	99.578
175	4.6784	3.4210	5.1256	99.569
195	4.6789	3.4213	5.1260	99.553
210	4.6797	3.4215	5.1266	99.540
225	4.6801	3.4219	5.1271	99.521
240	4.6805	3.4223	5.1276	99.507
255	4.6811	3.4229	5.1282	99.494
275	4.6814	3.4236	5.1287	99.473
295	4.6823	3.4242	5.1294	99.457
298	4.6823	3.4242	5.1294	99.457
323	4.6830	3.4252	5.1302	99.433
348	4.6834	3.4265	5.1317	99.401
373	4.6841	3.4276	5.1328	99.368
398	4.6849	3.4288	5.1338	99.339
423	4.6859	3.4300	5.1352	99.312
448	4.6867	3.4308	5.1363	99.285
473	4.6879	3.4318	5.1373	99.257
498	4.6887	3.4328	5.1387	99.225
523	4.6898	3.4337	5.1398	99.202
548	4.6909	3.4345	5.1409	99.175
573	4.6920	3.4352	5.1422	99.150
598	4.6933	3.4362	5.1432	99.127
623	4.6943	3.4372	5.1445	99.103
648	4.6958	3.4380	5.1458	99.078
673	4.6973	3.4387	5.1469	99.060
698	4.6989	3.4392	5.1481	99.044

The estimated standard uncertainties in the temperature T is $u(T) = 2$ K. The expanded, combined uncertainty at approximately 95 percent confidence limits in the values of a , b , c , and β is $U(x) = 0.002 \cdot x$.

Table 3. Lattice parameters a , b , c , and β of nanoscale CuO obtained from Rietveld analysis of XRD data collected at various temperatures from 90-700 °C.

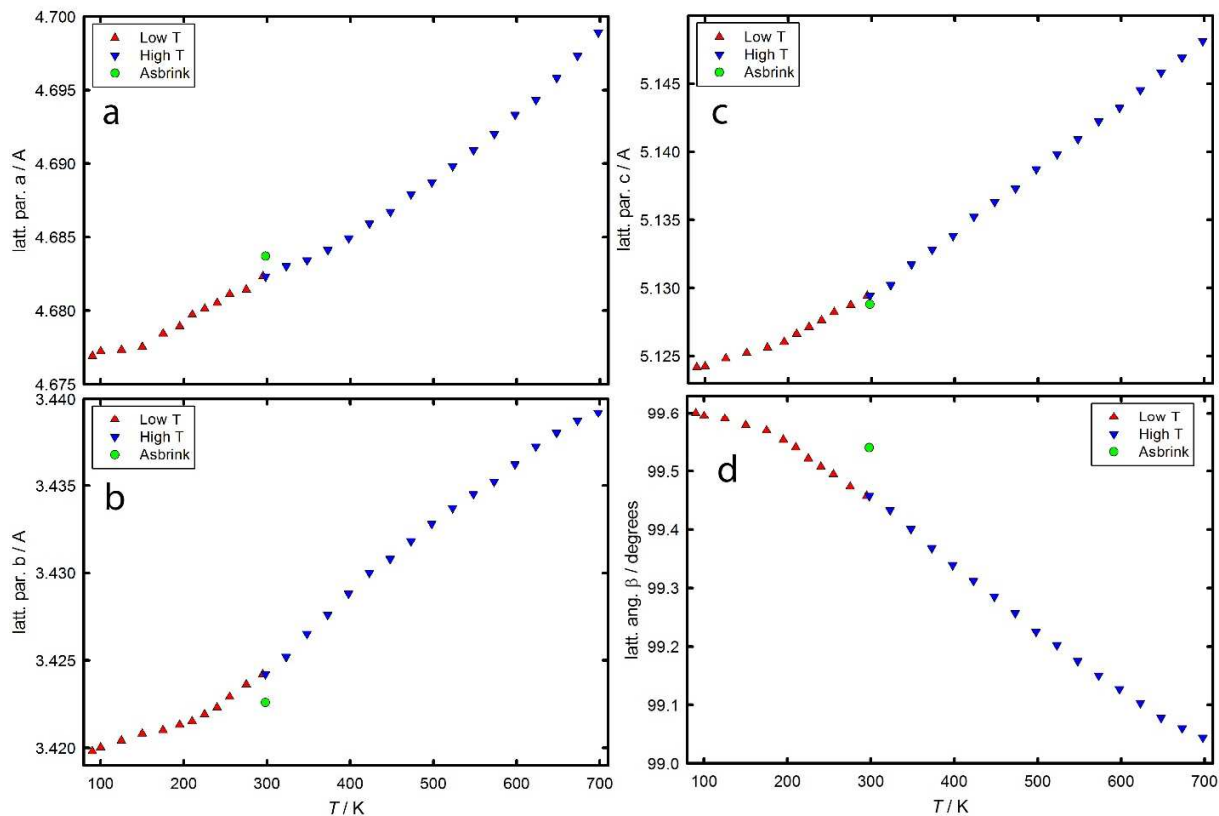


Figure 8. XRD lattice parameters of nanoscale CuO at various temperatures from 90-700 K as determined from a Rietveld refinement of the data shown in Figure 7. a) parameter a . b) parameter b . c) parameter c . d) parameter β . red triangles – low-temperature data. blue inverted triangles – high-temperature data. Units are in Å. Literature data (green circles) taken from Asbrink and Norrby [13].

The lowest temperature shift in lattice parameters occurs along the a axis at about 150 K. A shift in β occurs at about 170 K and in c at a slightly higher temperature of 195 K. The shift along the b axis occurs at the highest temperature of about 220 K. Other possible changes occur

at about 300 K and 400 K though these changes in slope are much more ambiguous and appear to occur over a wider temperature range than the slope changes at lower temperatures.

The changes in the a , b , and c lattice parameters at (150, 195, and 220) K, respectively, correspond to those of several other observed properties in bulk and nanoscale CuO. The shift in expansion of the a axis around 150 K appears to correspond to the minimum in magnetization. Charnaya *et al.* observed a decrease in T_{N1} to about 190 K in nanoscale CuO embedded in glass [43], which could be related to the shift in the c axis observed in this investigation. The change that occurs along b is also similar to the traditional T_{N2} observed at about 230 K. It is apparent that these shifts in lattice parameters and the corresponding structure are caused by the magnetic properties.

The relationship between structure and magnetic properties in bulk CuO has been established previously [20; 49; 50; 51]. Competition between ferromagnetic and antiferromagnetic interactions is known to cause structural distortions and even phase transitions [52]; therefore, the presence of these distortions in the lattice parameters of nanoscale CuO suggests that ferromagnetic behavior is significant and competes with the antiferromagnetic behavior. The presence of this strong ferromagnetic-antiferromagnetic competition in nanoscale CuO would therefore be expected to be different from the competition in bulk CuO since smaller particles tend to have larger unit cells (for metal oxides) due to reduced electrostatic forces caused by surface dipoles [53; 54], and these changes in the unit cell parameters affect the Cu–O–Cu bond angles that are highly correlated to the strength of the exchange interactions [17; 38].

3.3. Heat capacity analysis

The measured heat capacity data are given in Table 4 and shown graphically in Figure 9 for the low temperature and high temperature segments. Because the data of the two temperature

segments were collected using a different grease and addenda measurement, there was a slight offset of the high-temperature data from the low-temperature data. To correct for this offset, the high-temperature data that tend to have greater uncertainty were scaled by 1 % to match the low temperature data. Although the data for the two segments were collected with a 55 K overlap range (250-305 K), the temperature at which the two segments aligned in terms of heat capacity and the first derivative of the heat capacity data was taken as 295 K where deviations between the two sets of data were smallest. Data from the low-temperature segment above 295 K and from the high-temperature segment below 295 K were not used.

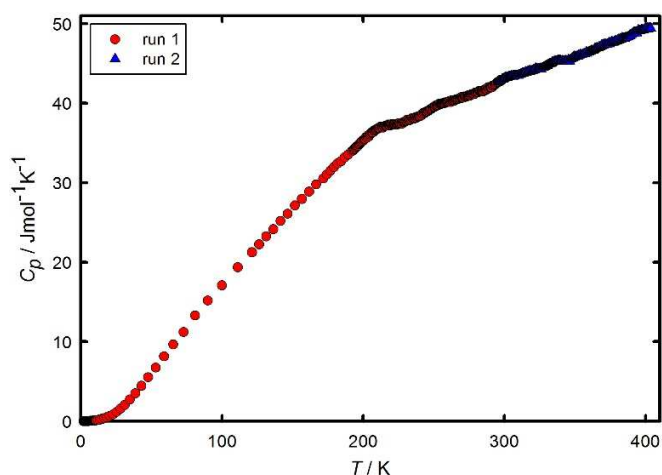


Figure 9. Raw heat capacity data of CuO nanoparticles. red circles – run 1 (low temperature data); blue triangles – run 2 (high temperature data).

T / K	$C_{p,m} / J \cdot K^{-1} \cdot mol^{-1}$	T / K	$C_{p,m} / J \cdot K^{-1} \cdot mol^{-1}$	T / K	$C_{p,m} / J \cdot K^{-1} \cdot mol^{-1}$	T / K	$C_{p,m} / J \cdot K^{-1} \cdot mol^{-1}$
1.834	1.62×10^{-3}	208.1	35.44	274.0	39.35	337.8	43.21
1.989	1.71×10^{-3}	208.6	35.51	274.6	39.38	338.3	43.21
2.143	1.97×10^{-3}	209.1	35.59	275.1	39.33	338.9	43.15
2.299	2.46×10^{-3}	209.6	35.60	275.6	39.37	339.4	43.14

2.452	2.67×10^{-3}	210.1	35.69	276.1	39.35	339.8	43.14
2.607	3.04×10^{-3}	210.6	35.73	276.6	39.50	340.3	43.10
2.794	3.68×10^{-3}	211.1	35.74	277.1	39.45	340.8	43.14
2.945	4.14×10^{-3}	211.6	35.75	277.7	39.54	341.3	43.02
3.087	4.48×10^{-3}	212.1	35.90	278.2	39.49	341.8	43.04
3.256	4.88×10^{-3}	212.6	35.86	278.7	39.50	342.3	43.11
3.397	5.34×10^{-3}	213.1	35.95	279.2	39.58	342.8	43.09
3.552	6.09×10^{-3}	213.6	35.90	279.7	39.70	343.3	43.14
3.710	7.06×10^{-3}	214.1	35.81	280.2	39.68	343.8	43.04
3.859	7.44×10^{-3}	214.6	35.92	280.7	39.74	344.3	43.12
4.005	8.77×10^{-3}	215.1	35.97	281.2	39.72	344.9	43.01
4.165	9.54×10^{-3}	215.6	36.02	281.7	39.73	345.4	43.23
4.317	0.01001	216.1	36.00	282.2	39.85	345.9	43.15
4.474	0.01094	216.6	36.02	282.7	39.85	346.4	43.02
4.630	0.01200	217.1	36.02	283.2	39.86	346.9	43.26
4.781	0.01282	217.7	36.14	283.7	39.86	347.5	43.31
4.933	0.01408	218.2	36.08	284.2	39.85	348.0	43.36
5.090	0.01472	218.7	36.08	284.7	39.88	348.5	43.39
5.236	0.01744	219.2	36.04	285.2	39.79	349.0	43.55
5.394	0.01840	219.7	36.08	285.7	39.87	349.5	43.55
5.548	0.01854	220.2	36.13	286.1	40.01	350.0	43.46
5.703	0.02191	220.7	36.21	286.7	40.03	350.5	43.54
5.855	0.02293	221.2	36.14	287.2	40.05	351.0	43.57
6.007	0.02325	221.7	36.15	287.7	39.99	351.5	43.56
6.160	0.02620	222.2	36.17	288.2	40.13	352.0	43.58
6.311	0.02834	222.7	36.20	288.7	40.28	352.5	43.71
6.454	0.03023	223.2	36.19	289.2	40.13	353.0	43.67
6.615	0.03252	223.7	36.10	289.7	40.23	354.0	43.82
6.769	0.03231	224.2	36.16	290.2	40.26	354.5	43.73
6.919	0.03633	224.7	36.15	290.7	40.25	355.0	43.69
7.072	0.03587	225.2	36.24	291.2	40.24	355.5	43.80
7.224	0.04004	225.7	36.24	291.8	40.45	356.0	43.82
7.376	0.04241	226.2	36.30	292.3	40.43	356.6	43.86
7.524	0.04162	226.7	36.21	292.8	40.52	357.1	43.82
7.680	0.04607	227.2	36.23	293.3	40.55	357.6	43.86
7.835	0.05014	227.7	36.21	293.7	40.61	358.1	44.06
7.984	0.04621	228.3	36.35	294.3	40.70	358.6	43.85
8.137	0.05536	228.8	36.39	294.8	40.79	359.1	43.96
8.293	0.06016	229.3	36.39	295.3	40.86	359.6	44.02
8.443	0.05748	229.8	36.47	295.8	40.89	360.1	44.05
8.592	0.06435	230.3	36.50	296.3	40.89	360.6	44.09
8.744	0.06557	230.8	36.55	296.8	41.04	361.1	44.10
8.896	0.07024	231.3	36.68	297.3	40.97	361.6	44.20
9.047	0.07547	231.8	36.59	295.4	40.90	362.1	44.17

9.200	0.07497	232.3	36.64	295.9	40.95	362.6	44.17
9.351	0.07630	232.8	36.60	296.4	41.00	363.1	44.18
9.504	0.08484	233.3	36.66	296.9	40.99	363.6	44.27
9.649	0.08092	233.8	36.74	297.4	41.02	364.1	44.39
9.804	0.09035	234.3	36.71	297.9	41.12	364.6	44.40
9.956	0.09086	234.8	36.83	298.4	41.19	365.1	44.46
10.11	0.09979	235.3	36.79	298.9	41.17	365.6	44.50
10.26	0.09955	235.8	36.73	299.4	41.25	366.1	44.44
10.37	0.1031	236.3	36.83	299.9	41.31	366.6	44.48
10.51	0.1061	236.8	36.87	300.5	41.34	367.1	44.61
10.66	0.1103	237.3	36.94	301.0	41.40	367.6	44.53
10.87	0.1150	237.8	36.86	301.5	41.34	368.1	44.63
12.07	0.1521	238.3	36.99	302.0	41.37	368.7	44.76
13.42	0.2037	238.8	36.97	302.5	41.42	369.2	44.70
14.91	0.2732	239.4	37.01	303.0	41.44	369.7	44.79
16.58	0.3639	239.9	37.03	303.5	41.48	370.2	44.76
18.41	0.4867	240.4	37.07	304.0	41.46	370.7	44.88
20.47	0.6477	240.9	37.19	304.5	41.48	371.2	44.83
22.78	0.8454	241.4	37.14	305.0	41.53	371.7	44.89
25.29	1.159	241.9	37.31	305.5	41.47	372.2	44.80
28.12	1.556	242.4	37.37	305.9	41.58	372.7	44.85
31.26	2.034	242.9	37.45	306.4	41.45	373.2	44.88
34.74	2.699	243.4	37.38	306.9	41.52	373.7	44.92
38.60	3.464	243.9	37.51	307.4	41.54	374.2	45.06
42.90	4.403	244.4	37.54	307.9	41.55	374.7	44.87
47.69	5.450	244.9	37.58	308.5	41.54	375.2	44.97
53.00	6.654	245.4	37.60	309.0	41.57	375.7	45.11
58.90	8.042	245.9	37.66	309.5	41.61	376.2	45.16
65.47	9.515	246.3	37.66	310.0	41.53	376.7	45.08
72.78	11.05	246.8	37.79	310.5	41.67	377.2	45.03
80.91	13.08	247.4	37.83	311.0	41.66	377.7	45.14
89.93	14.92	247.9	37.89	311.5	41.66	378.2	45.09
99.97	16.76	248.4	37.91	312.0	41.75	378.7	45.21
111.1	18.98	248.9	37.98	312.6	41.81	379.2	45.26
121.3	20.79	249.4	38.05	313.1	41.80	379.7	45.18
126.3	21.74	249.9	38.11	313.6	41.79	380.2	45.30
131.3	22.71	250.4	38.12	314.1	41.84	380.7	45.41
136.3	23.59	250.9	38.15	314.6	41.86	381.2	45.31
141.4	24.59	251.5	38.26	315.1	41.97	381.7	45.42
146.5	25.46	252.0	38.26	315.6	41.85	382.2	45.44
151.6	26.48	252.5	38.29	316.1	41.96	382.7	45.38
156.5	27.26	253.0	38.35	316.6	41.96	383.2	45.55
161.6	28.14	253.5	38.35	317.1	42.01	383.7	45.52
166.7	29.02	254.0	38.49	317.6	42.10	384.2	45.52
171.7	29.72	254.5	38.46	318.1	41.92	384.7	45.53

174.2	30.21	255.0	38.43	318.6	42.10	385.2	45.46
176.8	30.66	255.5	38.50	319.1	42.02	385.7	45.56
179.3	31.10	256.0	38.51	319.6	42.10	386.2	45.54
181.8	31.52	256.5	38.52	320.2	42.07	386.7	45.59
184.3	31.81	257.0	38.55	320.7	42.19	387.3	45.64
186.9	32.25	257.5	38.52	321.2	42.17	387.8	45.58
189.4	32.62	258.0	38.61	321.7	42.10	388.3	45.69
191.9	32.97	258.5	38.61	322.1	42.36	388.8	45.81
192.9	33.09	258.9	38.62	322.6	42.20	389.3	45.70
193.4	33.21	259.4	38.66	323.1	42.23	389.8	45.93
193.9	33.30	259.9	38.65	323.6	42.24	390.3	45.88
194.4	33.39	260.4	38.69	324.1	42.30	390.8	46.01
194.9	33.47	260.9	38.68	324.6	42.27	391.3	45.97
195.4	33.56	261.5	38.77	325.1	42.28	391.8	46.18
196.0.	33.57	262.0	38.65	325.6	42.33	392.3	46.16
196.5	33.66	262.5	38.80	326.1	42.23	392.8	46.15
197.0	33.80	263.0	38.78	326.6	42.35	393.3	46.15
197.5	33.86	263.5	38.80	327.1	42.35	393.8	46.05
198.0	33.95	264.0	38.84	327.6	42.39	394.3	46.28
198.5	34.08	264.5	38.78	328.1	42.43	394.8	46.40
199.0	34.15	265.1	38.86	328.6	42.50	395.3	46.35
199.5	34.28	265.5	38.93	329.2	42.55	395.8	46.34
200.0	34.27	266.1	38.94	329.8	42.61	396.3	46.27
200.5	34.39	266.6	38.95	330.3	42.59	396.8	46.34
201.0	34.44	267.1	38.99	330.8	42.73	397.3	46.39
201.5	34.47	267.6	38.98	331.3	42.73	397.8	46.42
202.0	34.67	268.1	39.07	331.8	42.85	398.3	46.32
202.5	34.59	268.6	39.04	332.3	42.82	398.8	46.34
203.0	34.73	269.1	39.15	332.8	42.83	399.3	46.52
203.5	34.86	269.6	39.19	333.3	42.88	399.9	46.59
204.0	34.75	270.1	39.08	333.8	43.01	400.4	46.51
204.5	34.92	270.6	39.11	334.3	42.99	400.9	46.47
205.0	35.00	271.1	39.11	334.8	43.02	401.4	46.59
205.5	35.16	271.6	39.27	335.3	43.06	401.9	46.43
206.0	35.24	272.0	39.26	335.8	43.12	402.4	46.62
206.5	35.21	272.5	39.23	336.3	43.05	402.9	46.52
207.0	35.27	273.0	39.27	336.8	43.08	403.4	46.58
207.6	35.45	273.6	39.28	337.3	43.11	403.9	46.51

The estimated, combined standard uncertainties in the temperature T and pressure p are $u(T) = 0.001 \cdot T/K$ and $u(p) = 0.10$ mPa. The expanded, combined uncertainties at approximately 95 percent confidence limits in the values of $C_{p,m}^{\circ}$ are $U(C_{p,m}^{\circ}) = 0.06 \cdot C_{p,m}^{\circ}$ ($2 < T/K < 10$), $U(C_{p,m}^{\circ}) = 0.01 \cdot C_{p,m}^{\circ}$ ($10 < T/K < 295$), and $U(C_{p,m}^{\circ}) = 0.02 \cdot C_{p,m}^{\circ}$ ($295 < T/K < 405$).

Table 4. Measured molar heat capacity data at constant pressure ($p = 1.2$ mPa) for $\text{CuO} \cdot 0.05\text{H}_2\text{O}$. $M = 80.446$ g·mol⁻¹. Data below 295 K were collected with the sample thermally attached to the calorimeter using Apiezon N grease; data above 295 K were collected with the sample attached using Apiezon H grease.

Figure 10 below shows how our heat capacity data of nanoscale CuO compare with data found in the literature for bulk CuO. Data are shown just around the observed T_{N1} and T_{N2} bulk CuO transition temperatures since the literature data do not extend much higher in temperature. The somewhat noisy and diffuse data of Millar show a broad transition peaked at about 230 K [21]. The data of Junod *et al.* are the most precise and show distinct and sharp transitions at 215 K, 230 K, and 235 K, though the transition at 235 K is attributed to the silicone grease used to mount the sample [4]. The data by Seehra *et al.* show two broad transitions that overlap having maxima at about 217 K and 230 K [3]. In general, the literature data of bulk CuO show a distinct first-order transition at about 213 K and a broader transition at about 230 K.

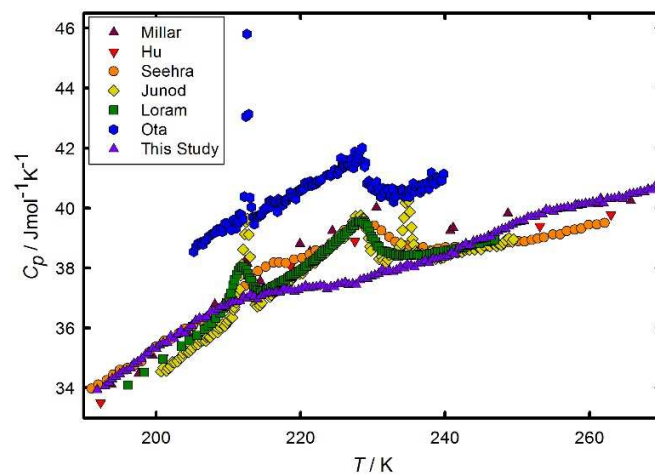


Figure 10. Heat capacity data of nanoscale CuO from 180 to 320 K compared to data of bulk CuO from the literature. maroon triangles – Millar [21]; red inverted triangles – Hu *et al.* [22]; orange circles – Seehra *et al.* [3]; yellow diamonds – Junod *et al.* [4]; green squares – Loram *et al.* [2]; blue hexagons – Ota *et al.* [27]; purple triangles – this study.

Our data, however, show very broad transitions at temperatures quite different from the bulk transitions. As can be seen in Figures 9 and 10, our data show four subtle transitions at about (210, 250, 300, and 330) K. These transitions are likely much broader than those of bulk CuO due to chemical impurities and particle size inhomogeneity. The extra transitions at 300 and 330 K not present in other data could be a result of anomalies in heat capacity of the Apiezon N and Apiezon H greases, which are known to have transitions in this region – albeit usually less defined and reproducible [55; 56; 57]. To understand the heat capacity data and the transitions more fully, we analyzed the heat capacity data and subtracted the lattice heat capacity from the total heat capacity to reveal just the magnetic heat capacity.

3.3.1. Heat Capacity Data Fitting

Prior to analysis of the heat capacity data, we first corrected for the amount of water present on the surface of the CuO nanoparticles as well as the difference between the measured C_p and the more theoretically important C_v . The correction from C_p to C_v was performed using the Nernst-Lindemann equation [58]:

$$C_v = C_p - AC_p^2T \quad (1)$$

where A equals $1.35 \times 10^{-6} \text{ J}\cdot\text{mol}^{-1}$ assuming a linear expansion coefficient at 300 K of 10^{-5} K^{-1} using the values used previously for bulk CuO by others [2; 4; 58]. This correction resulted in a change of less than 1 % below 200 K and a maximum change of 2.6 % at 400 K.

The correction for water tends to be much less straightforward. We have recently summarized and discussed various surface-adsorbed water heat capacity models that have been published in the literature [59]. A recent investigation using neutron techniques derived the heat capacity of the CuO surface-adsorbed water [60]. Although this water model might appear to be the best representation for the water on our CuO samples, that study involved a sample with ten times more water than ours suggesting that they measured mostly physisorbed water; whereas, we measured only chemisorbed water. Because of this, we chose to use the “inner TiO₂” water model, which has proven to be applicable to several similar systems involving only chemisorbed water [59].

After these corrections, the low temperature ($T < 10 \text{ K}$) heat capacity data were fit to several theoretical functions that provide information on the various contributions to the heat capacity. The best fitting function was determined from the percent root mean square deviation (%RMS) and a plot of the deviation of each point from the fitting function. The fit that was physically meaningful had the lowest %RMS, and had random deviations was selected as the best fit.

The heat capacity data below 10 K were fit to the sum of theoretical functions:

$$C_{low T} = \gamma T + B_3 T^3 + B_5 T^5 \quad (2)$$

where the γ term represents the contribution from lattice vacancies [46] or 1D antiferromagnetic spin waves [4], and the B_3 and B_5 terms are coefficients of the series expansion of the Debye harmonic crystal lattice heat capacity [61]. Several studies have shown that a contribution from 2-dimensional surface phonons, proportional to T^2 , becomes distinguishable in nanoparticles due to the large number of surface atoms relative to bulk atoms [58; 62; 63]; however, no such term is needed for this sample. This could be a result of the particle size (~ 20 nm) and the particles agglomerating so closely that the surface phonons are disrupted by the presence of other particles nearby. These particle boundaries would behave similar to lattice vacancies which would account for the relatively large linear term, γ , produced from lattice vacancies. These low-temperature fit parameters and their corresponding %RMS are given in Table 5.

$\gamma / \text{mJ}\cdot\text{mol}^{-1}\cdot\text{K}^{-2}$	0.489
$B_3 / \text{mJ}\cdot\text{mol}^{-1}\cdot\text{K}^{-4}$	0.102
$B_5 / \text{mJ}\cdot\text{mol}^{-1}\cdot\text{K}^{-6}$	-1.29E-4
%RMS	3.26

Table 5. Low temperature ($T < 10$ K) heat capacity fit parameters.

Samples that are antiferromagnetic also have a T^3 dependence; therefore, to distinguish between the lattice and antiferromagnetic T^3 , the Debye temperature, which can give the lattice contribution, must be known. The B_3 coefficient shown in Table 5 is not significantly different from that derived from the bulk CuO Debye temperature of 390 K ($0.07 \text{ mJ}\cdot\text{mol}^{-1}\cdot\text{K}^{-4}$) from Junod *et al.* [4]. The antiferromagnetic T^3 term is typically ten to twenty times larger than the phonon T^3 term [58]; therefore, this B_3 term does not appear to show any significant

antiferromagnetic contribution below 10 K, which is similar to other low-temperature heat capacity investigations [4; 24].

3.3.2. Magnetic Transitions

The magnetic heat capacity transitions of our nanoscale CuO sample (with the water contribution subtracted) were determined by subtracting the lattice contribution from the total heat capacity, as has been done by Junod *et al.* and Loram *et al.*, using the bulk CuO lattice data determined from neutron experiments [2; 4]. Figure 11 shows the magnetic heat capacity transitions of our nanoscale CuO as well as bulk CuO data from Junod *et al.* [4] and Loram *et al.* [2]

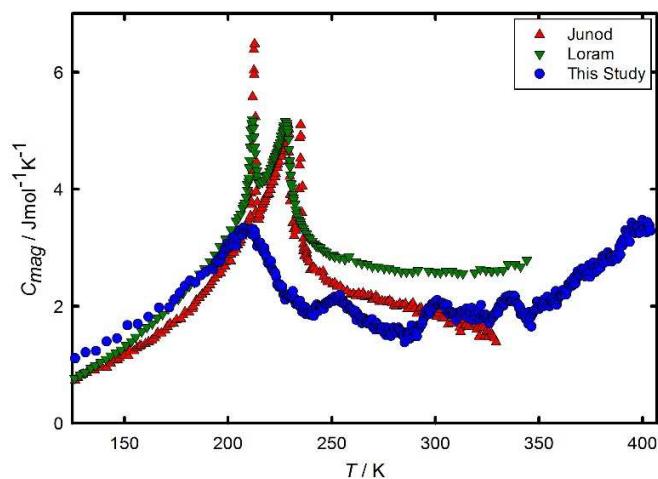


Figure 11. Magnetic heat capacity transitions of our nanoscale CuO sample from 125-405 K in comparison to the magnetic heat capacity transitions of bulk CuO from the literature. red triangles – Junod *et al.* [4]; green inverted triangles – Loram *et al.* [2]; blue circles – this study.

As seen in Figure 11, the magnetic heat capacity data of our nanoscale CuO show four transitions, three of which occur at temperatures that are higher than the transitions reported by

Junod *et al.* and Loram *et al.* [2; 4]. The transitions in our nanoscale CuO are much more visible after the lattice has been subtracted (compare to Figures 9 and 10). The high-temperature “tail” of the transition in the bulk CuO data of Junod *et al.* decreases with increasing temperature [4], but the tail in the bulk CuO data or Loram *et al.* levels off and appears to increase above about 300 K [2]. In our nanoscale CuO sample, the tail increases significantly above the fourth transition at about 350 K. Loram *et al.* attributed this tail above T_{N2} to 1D magnetism since a large tail is a result of a lower dimensionality [4].

Thermodynamic data at the transition temperatures were generated by fitting the data in Figure 11 with a cubic spline function and integrating. The entropies and enthalpies of the transitions as well as the transition peak temperatures are given in Table 6. The entropies of these transitions can be used to identify the dimensionality of the magnetic character since the entropy at T_{N2} is predicted to be about $0.3R \ln 2$ ($1.73 \text{ J}\cdot\text{mol}^{-1}\cdot\text{K}^{-1}$) for a 1D magnetic system and about $0.12R \ln 2$ ($0.69 \text{ J}\cdot\text{mol}^{-1}\cdot\text{K}^{-1}$) for a 2D system [2; 4]. Because our entropies ($> 0.5R \ln 2$) are significantly higher than either of these values and are closer to those of a 3D, spin $\frac{1}{2}$ Heisenberg antiferromagnet [64], we believe that the competing ferromagnetic interactions are more significant for these nanoparticles and cause an increase in the entropy of the transitions.

$T /$ K	$\Delta_o^T S_{trans}^o /$ $\text{J}\cdot\text{K}^{-1}\cdot\text{mol}^{-1}$	$\Delta_o^T H_{trans}^o /$ $\text{J}\cdot\text{mol}^{-1}$
208.6	2.649 ± 0.026	271.7 ± 2.7
251.9	3.104 ± 0.031	375.0 ± 3.8
302.6	3.426 ± 0.069	464.1 ± 9.3
335.9	3.626 ± 0.072	529 ± 11

Table 6. Magnetic transition temperatures, entropies, and enthalpies.

As seen in Table 6, the nanoscale CuO sample has peaks at (208.6, 251.9, 302.6, and 335.9) K. Only the peak at 208.6 K resembles the transition between the AF1 and AF2 phases in the bulk CuO phases. As such, the transition from incommensurate to 1D antiferromagnetism at 230 K is not observed, though it is reasonable to assume that this transition is manifest in the higher temperature transitions; however, neutron experiments on the magnetic properties at these temperatures is necessary to definitively determine the state of the magnetic order between the transitions. Although it has been shown that external magnetic fields do not induce changes in the temperature ranges of multiferroicity [11], Rocquefelte *et al.* have used density functional theory and Monte Carlo calculations to show that at high pressures, the multiferroic state of CuO can extend from 230 K up to about 300 K [65]. Because the higher pressures would affect the lattice parameters and cause this increase in the multiferroic temperature range, it is reasonable to suggest that our sample, having multiple lattice distortions, also has an extended range of multiferroicity or of the AF2 phase.

The number of transitions observed in the heat capacity data of nanoscale CuO does not correspond to those determined for bulk CuO that report only two, although Villarreal *et al.* have reported that the transition at 230 K actually consists of two transitions very close in temperature making a total of three transitions [19]. Competition between antiferromagnetic and ferromagnetic interactions in bulk CuO are known to cause the multiple transitions associated with the AF1 and AF2 states [30; 35; 38]; therefore, it is reasonable to assume that changes in the degree of magnetic competition could induce changes in those transitions, and the non-cooperative shifts in lattice parameters could result in additional regions of ferroic order and therefore more transitions.

5. Conclusions

From magnetization measurements it was shown that nanoscale CuO exhibits similar susceptibility to that of bulk with the most significant differences being the higher concentration of paramagnetic centers in the form either of surface sites or lattice vacancies as well as stronger ferromagnetic interactions. The XRD data revealed that the CuO lattice parameters do not increase smoothly with temperature but rather have several critical temperatures at which their slope changes significantly; furthermore, these changes in the lattice parameters occur at different temperatures for each of the different parameters. Because these temperatures are similar to known magnetic transitions, we have shown how each magnetic region is related to structural features along the different axes. Heat capacity data revealed that the traditional transitions observed in bulk CuO are significantly altered in nanoscale CuO. The temperature ranges of the various magnetic and ferroelectric domains increase to higher temperatures, and new domains were observed.

We have shown that structural features in the CuO lattice unique to nanoparticles can induce changes in the multiferroic AF2 state. Specifically, the structure of the lattice and the various Cu–O–Cu bond distances and angles are significant in forming competing ferromagnetic and antiferromagnetic interactions. This competition causes the multiferroicity to appear at different temperatures. From an applications viewpoint, this investigation shows that CuO nanoparticles could be a possible candidate for room temperature multiferroic devices.

Acknowledgements

We would like to thank Dr. Stacey Smith for help with the XRD experiments and Dr. Jeff Farrer and Paul Minson for their help with the TEM imaging. Funding for this work was provided by the U.S. Department of Energy under grant DE-FG02-05ER15666.

REFERENCES

- [1] M. O'Keefe, F. Stone, *Journal of Physics and Chemistry of Solids* 23 (1962) 261-266.
- [2] J. Loram, K. Mirza, C. Joyce, A. Osborne, *EPL (Europhysics Letters)* 8 (1989) 263.
- [3] M.S. Seehra, Z. Feng, R. Gopalakrishnan, *Journal of Physics C: Solid State Physics* 21 (1988) L1051.
- [4] A. Junod, D. Eckert, G. Triscone, J. Müller, W. Reichardt, *Journal of Physics: Condensed Matter* 1 (1989) 8021.
- [5] K. Zhou, R. Wang, B. Xu, Y. Li, *Nanotechnology* 17 (2006) 3939.
- [6] D. Chauhan, V. Satsangi, S. Dass, R. Shrivastav, *Bulletin of Materials Science* 29 (2006) 709.
- [7] Q. Bao, C.M. Li, L. Liao, H. Yang, W. Wang, C. Ke, Q. Song, H. Bao, T. Yu, K.P. Loh, *Nanotechnology* 20 (2009) 065203.
- [8] C. Wadia, A.P. Alivisatos, D.M. Kammen, *Environmental Science & Technology* 43 (2009) 2072-2077.
- [9] X. Gao, J. Bao, G. Pan, H. Zhu, P. Huang, F. Wu, D. Song, *The Journal of Physical Chemistry B* 108 (2004) 5547-5551.
- [10] T. Kimura, Y. Sekio, H. Nakamura, T. Siegrist, A. Ramirez, *Nature materials* 7 (2008) 291-294.
- [11] F. Wang, T. Zou, Y. Liu, L.-Q. Yan, Y. Sun, *Journal of Applied Physics* 110 (2011) 054106.
- [12] P. Babkevich, A. Poole, R.D. Johnson, B. Roessli, D. Prabhakaran, A.T. Boothroyd, *Physical Review B* 85 (2012) 134428.
- [13] S. Åsbrink, L.-J. Norrby, *Acta Crystallographica Section B: Structural Crystallography and Crystal Chemistry* 26 (1970) 8-15.
- [14] N. Brese, M. O'Keefe, B. Ramakrishna, R. Von Dreele, *Journal of Solid State Chemistry* 89 (1990) 184-190.
- [15] W. Wu, N. Hiraoka, D. Huang, S. Huang, K. Tsuei, M. van Veenendaal, J. van den Brink, Y. Sekio, T. Kimura, *Physical Review B* 88 (2013) 205129.
- [16] B. Yang, J. Tranquada, G. Shirane, *Physical Review B* 38 (1988) 174.
- [17] B.X. Yang, T.R. Thurston, J.M. Tranquada, G. Shirane, *Physical Review B* 39 (1989) 4343-4349.
- [18] E. Gmelin, *Indian Journal of Pure and Applied Physics* 30 (1992) 596-608.
- [19] R. Villarreal, G. Quirion, M. Plumer, M. Poirier, T. Usui, T. Kimura, *Physical review letters* 109 (2012) 167206.
- [20] A. Rebello, Z.C.M. Winter, S. Viall, J.J. Neumeier, *Physical Review B* 88 (2013) 094420.
- [21] R.W. Millar, *Journal of the American Chemical Society* 51 (1929) 215-222.
- [22] J.-H. Hu, H.L. Johnston, *Journal of the American Chemical Society* 75 (1953) 2471-2473.
- [23] H.H. Kellogg, *Journal of Chemical & Engineering Data* 14 (1969) 41-44.
- [24] A. Junod, D. Eckert, G. Triscone, J. Muller, W. Reichardt, *Physica C: Superconductivity* 162 (1989) 478-479.
- [25] E. Gmelin, U. Köbler, W. Brill, T. Chattopadhyay, S. Sastry, *Bulletin of Materials Science* 14 (1991) 117-123.
- [26] S. Ota, E. Gmelin, *Journal of Thermal Analysis and Calorimetry* 38 (1992) 635-640.

- [27] S.B. Ota, E. Gmelin, *Physical Review B* 46 (1992) 11632-11635.
- [28] B.-X. Wang, L.-P. Zhou, X.-F. Peng, *International Journal of Thermophysics* 27 (2006) 139-151.
- [29] K. Saito, S. Ikeuchi, Y. Nakazawa, X.-G. Zheng, M. Brian Maple, M. Sorai, *Solid State Communications* 125 (2003) 23-26.
- [30] R. Borzi, S. Stewart, G. Punte, R. Mercader, R. Zysler, M. Tovar, *Solid state communications* 117 (2001) 311-314.
- [31] H. Bizette, B. Tsai, *Comptes Rendus Hebdomadaires des Seances de L Academie des Sciences* 241 (1955) 182-188.
- [32] A. Punnoose, H. Magnone, M. Seehra, J. Bonevich, *Physical Review B* 64 (2001) 174420.
- [33] V. Bisht, K. Rajeev, S. Banerjee, *Solid State Communications* 150 (2010) 884-887.
- [34] S. Rehman, A. Mumtaz, S.K. Hasanain, *J Nanopart Res* 13 (2011) 2497-2507.
- [35] M. Mekata, N. Yaguchi, T. Takagi, T. Sugino, S. Mitsuda, H. Yoshizawa, N. Hosoi, T. Shinjo, *Journal of the Physical Society of Japan* 62 (1993) 4474-4487.
- [36] J.B. Forsyth, P.J. Brown, B.M. Wanklyn, *Journal of Physics C: Solid State Physics* 21 (1988) 2917.
- [37] M. Ain, A. Menelle, B. Wanklyn, E. Bertaut, *Journal of Physics: Condensed Matter* 4 (1992) 5327.
- [38] H.J. Koo, M.H. Whangbo, *Inorganic Chemistry* 42 (2003) 1187-1192.
- [39] C.E. Housecroft, A.G. Sharpe, *Inorganic Chemistry*, Pearson, 2012.
- [40] T. Shimizu, T. Matsumoto, A. Goto, K. Yoshimura, K. Kosuge, *Journal of the Physical Society of Japan* 72 (2003) 2165-2168.
- [41] N. Ortega, A. Kumar, J. Scott, R.S. Katiyar, *Journal of Physics: Condensed Matter* 27 (2015) 504002.
- [42] A. Viano, S.R. Mishra, R. Lloyd, J. Losby, T. Gheyi, *Journal of Non-Crystalline Solids* 325 (2003) 16-21.
- [43] E. Charnaya, M. Lee, C. Tien, V. Pak, D. Formus, A. Pirozerskii, A. Nedbai, E. Ubyivovk, S. Baryshnikov, L. Chang, *Journal of Magnetism and Magnetic Materials* 324 (2012) 2921-2925.
- [44] M.A. Dar, Y.S. Kim, W.B. Kim, J.M. Sohn, H.S. Shin, *Applied Surface Science* 254 (2008) 7477-7481.
- [45] B.F. Woodfield, S. Liu, J. Boerio-Goates, Q. Liu, S.J. Smith, Preparation of uniform nanoparticles of ultra-high purity metal oxides, mixed metal oxides, metals, and metal alloys, US Patent Database, Brigham Young University, United States, 2012, pp. 1-22.
- [46] J.M. Schliesser, B.F. Woodfield, *Physical Review B* 91 (2015) 024109.
- [47] Q. Shi, J. Boerio-Goates, B.F. Woodfield, *The Journal of Chemical Thermodynamics* 43 (2011) 1263-1269.
- [48] R. Stevens, J. Boerio-Goates, *The Journal of Chemical Thermodynamics* 36 (2004) 857-863.
- [49] A. Kuz'menko, D. Van der Marel, P. Van Bentum, E. Tishchenko, C. Presura, A. Bush, *Physical Review B* 63 (2001) 094303.
- [50] B. Himmetoglu, R.M. Wentzcovitch, M. Cococcioni, *Physical Review B* 84 (2011) 115108.
- [51] D. Dai, H.-J. Koo, M.-H. Whangbo, *Inorganic chemistry* 43 (2004) 4026-4035.

- [52] N. Tristan, V. Zestrea, G. Behr, R. Klingeler, B. Büchner, H.K. von Nidda, A. Loidl, V. Tsurkan, *Physical Review B* 77 (2008) 094412.
- [53] M. Ghosh, D. Karmakar, S. Basu, S. Jha, D. Bhattacharyya, S. Gadkari, S. Gupta, *Journal of Physics and Chemistry of Solids* 75 (2014) 543-549.
- [54] M.I. Ahmad, S. Bhattacharya, *Applied Physics Letters* 95 (2009) 1906.
- [55] J. Bunting, T. Ashworth, H. Steeple, *Cryogenics* 9 (1969) 385-386.
- [56] M. Kreitman, T. Ashworth, M. Rechowicz, *Cryogenics* 12 (1972) 32-34.
- [57] E. Westrum, C. Chou, D. Osborne, H. Flotow, *Cryogenics* 7 (1967) 43-44.
- [58] E.S.R. Gopal, *Specific heats at low temperatures*, Plenum Press New York, 1966.
- [59] J.M. Schliesser, B. Huang, S.K. Sahu, A. Navrotsky, B.F. Woodfield, *Journal of Physical Chemistry C* (2016).
- [60] E.C. Spencer, N.L. Ross, S.F. Parker, R.E. Olsen, B.F. Woodfield, *Chemical Physics* 427 (2013) 66-70.
- [61] N.E. Phillips, *Critical Reviews in Solid State and Material Sciences* 2 (1971) 467-553.
- [62] E.W. Montroll, *The Journal of Chemical Physics* 18 (1950) 183-185.
- [63] D. Patterson, J. Morrison, F. Thompson, *Canadian Journal of Chemistry* 33 (1955) 240-244.
- [64] L.J. de Jongh, A.R. Miedema, *Advances in Physics* 23 (1974) 1-260.
- [65] X. Rocquefelte, K. Schwarz, P. Blaha, S. Kumar, J. van den Brink, *Nat Commun* 4 (2013).